ACS APPLIED MATERIALS & INTERFACES

Research Article

Cite This: ACS Appl. Mater. Interfaces 2020, 12, 2087−2094

www.acsami.org

Target-Driven Cascade-Amplified Release of Loads from DNA-Gated Metal−Organic Frameworks for Electrochemical Detection of Cancer Biomarker

Ting Bao, Ruobing Fu, Wei Wen, Xiuhua Zhang, and Shengfu Wang*

Hubei Collaborative Innovation Center for Advanced Organic Chemical Materials, Ministry of Education Key Laboratory for the Synthesis and Application of Organic Functional Molecules & College of Chemistry and Chemical Engineering, Hubei University, Wuhan 430062, PR China

Supporting Information

ABSTRACT: In this paper, a label-free and stimuli-responsive electrochemical biosensing platform was fabricated based on target-driven load release from DNA-gated metal−organic frameworks (MOFs) with cascade amplification. By using MOFs (UiO-66-NH_2) as a nanocarrier of electroactive molecules (methylene blue; MB) and the programmably assembled DNA acted as the gatekeeper, the biofunctionalized MOFs (MB@DNA/MOFs) were not only used as an amplified signal label but also worked as three-dimensional tracks for biosensing. In the presence of a target, the nicking endonuclease cleavage process was triggered, leading to the generation of two strands (S1 and S2). Both S1 and S2 act as stimuli to participate in the strand displacement reaction on the MB@DNA/MOFs, which caused the unlocking of the pore to release MB, resulting in the decrease of the signal. Using carcinoembryonic antigen (CEA) as a model target, the cascade-amplified biosensor presented good performance for CEA detection, ranging from 50 fg/mL to 10 ng/mL with a detection limit of 16 fg/mL. The stimuli-responsive DNA-gated MOF-based electrochemical platform exhibited three-dimensional biosensing tracks with rational utilization of the cascade amplification, providing an effective method for cancer biomarker detection.

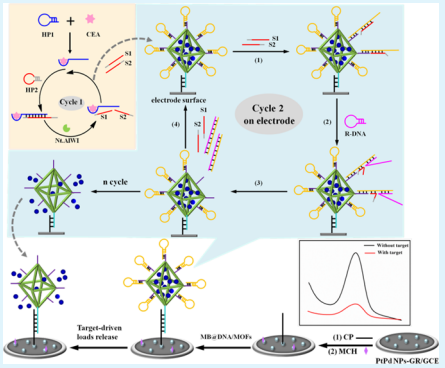

KEYWORDS: *electrochemical biosensor, stimuli-responsive platform, DNA-gated MOFs, carcinoembryonic antigen, target-driven load release, cascade amplification strategy*

INTRODUCTION

Cancer, as a kind of disease with high lethality, has become the leading cause of global deaths in recent years.[1] Realization of early and accurate diagnosis is distinctly important for the cancer therapy with the worldwide increase of cancer incidence. Cancer biomarkers can monitor the progression of cancer and contribute to early diagnosis; thus, it is significant to develop a sensitive biosensing platform for these biomarkers.[2,3] To improve the sensitivity, different biosensing tracks with various DNA nanotechnology including hybridization chain reaction (HCR), nuclease cleavage amplification, metal ion-dependent DNAzyme, rolling circle amplification (RCA), and strand displacement reaction (SDR) have been involved for signal amplification.[4−9] However, these processes are commonly performed on one-dimensional or two-dimensional tracks, which astrict the amplification efficiency. Nanomaterials can be introduced to construct higher dimensional tracks, which are beneficial to amplify the signal with a high specific surface area, providing more loading sites for DNA tracks.

Metal−organic frameworks (MOFs) are porous materials coordinated by metal ions and organic linkers, which have attracted substantial attention with a large specific surface area, high porosity, and chemical stability.[10,11] The prominent properties of MOFs enabled their wide application in gas adsorption and separation, catalysis, drug delivery, and biosensing field.[12−15] As to the MOF-based biosensing system, the large specific surface area and chemical functional group of MOFs provide plentiful sites for biomolecule immobilization, including aptamer, antibodies, and polypeptide, which can recognize a broad range of targets.[16−18] Besides, MOFs also can be used as a catalyst through acting as a substrate to anchor enzymes, signal molecules, and catalytic nanoparticles, which are conducive to produce an amplified signal.[19−21] Therefore, MOFs have become a promising material in the construction of a different biosensing system.

Owing to the multifunctional features as molecular recognition and building block elements,[22,23] DNA nanostructures are smart components to be introduced into MOFs (DNA/MOFs), which endow MOFs with a stimuli-responsive ability. The abundant and highly ordered pores endow MOFs the ability to act as nanocarriers for signal molecules, with the

Received: October 17, 2019
Accepted: December 17, 2019
Published: December 17, 2019

DOI: 10.1021/acsami.9b18805
ACS Appl. Mater. Interfaces 2020, 12, 2087−2094

DNA self-assembly with high programmability, structural diversity, and good biological properties acting as effective gatekeepers for the encapsulation of loads into the pore of MOFs, which are beneficial to produce a prominent signal. In the presence of specific stimuli, the DNA capping units can specifically recognize the target to form a capping DNA target complex, which performs various conformation switches with the conversion to different structures, including G-quadruplex, double helix, DNA dendrimers, and so on.[24] Ultimately, the capping DNA is unwinded and then dissociated from the surface of MOFs, resulting in the unlocking of the pore and the release of the loads.[25−27] Owing to the fact that DNA/MOFs possess both molecular recognition and signal output ability, which are favorable for the development of a fascinating biosensing platform. Generally, the stimuli-responsive DNA/MOF biosensing systems often directly use the targets as stimuli, and no other signal amplification strategies are introduced, which limit the release effect of the loads and affect the sensitivity of the biosensor. Therefore, it is significant to develop the three-dimensional DNA/MOF biosensing tracks integrated with rational utilization of a cascade amplification strategy, which is conducive to construct a biosensing platform with high sensitivity.

In this work, a label-free and ultrasensitive electrochemical biosensing platform was designed based on DNA-gated MOFs integrated with target-driven cascade amplification for load release. The MOFs (UiO-66-NH_2) were used as effective nanocarriers for both the programmable DNA assembly and the signal molecule (methylene blue; MB) loading to form MB@DNA/MOFs, which realized an amplified signal output. The presence of a target initiated the nicking endonuclease cleavage and SDR process, which caused unlocking of the pores to release the signal molecule. Using carcinoembryonic antigen (CEA) as a model target, the proposed biosensor provided a sensitive and effective strategy for the detection of CEA, holding potential application in cancer diagnosis.

EXPERIMENTAL SECTION

Materials and Reagents. Carcinoembryonic antigen (CEA), tris(2-carboxyethyl)phosphinehydrochloride (TCEP), and mercapto-1-hexanol (MCH) were provided by Sigma-Aldrich LLC. (St. Louis, USA). $ZrCl_4$, aminoterephthalic acid (NH_2-BDC), *N*-(3-dimethylaminopropyl)-*N*′-ethylcarbodiimide hydrochloride (EDC), hydrogen hexachloroplatinate(IV) hexahydrate ($H_2PtCl_6{\cdot}6H_2O$), potassium hexachloropalladate(IV) (K_2PdCl_6), *N*-hydroxysulfosuccinimide sodium salt (NHS), methylene blue (MB), *N*,*N*-dimethylformamide (DMF), and hemoglobin (HB) were purchased from Aladdin Chemical Co. (Shanghai, China). Immunoglobulin G (IgG), human serum albumin (HSA), and thrombin (TB) were received from Yuanye Bio-Technology Co., Ltd. (Shanghai, China). Graphene was received from Sinocarbon Materials Technology Co., Ltd. (Shanxi, China). Nicking endonuclease (Nt.AlwI) was obtained from the New England Biolabs (Beijing China). All other chemicals in the experiment were analytical grade. Oligonucleotides including hairpin DNA1 (HP1), hairpin DNA2(HP2), capture probe (CP), binding DNA1 (B-DNA1), binding DNA2 (B-DNA2), lock DNA (L-DNA), and replacement DNA (R-DNA) were ordered from Sangon Biotechnology Co., Ltd. (Shanghai, China); the sequences are listed in Table S1. Prior to use, HP1, HP2, L-DNA, and R-DNA were kept at 95 °C for 5 min and slowly cooled down to form a hairpin structure.

Apparatus and Measurements. For electrochemical measurements, a CHI 660E electrochemical workstation (Shanghai CH Instruments, China) with a three-electrode system constituted by a saturated calomel electrode (SCE), a platinum wire, and a modified glassy carbon electrode (GCE) were exploited. Differential pulse voltammetry (DPV) was detected in Tris−HCl (20 mM, pH 7.4), ranging from −0.6 to 0 V. Electrochemical impedance spectroscopy (EIS) was carried out in 5 mM $[Fe(CN)_6]^{3-/4-}$ solution containing 0.1 M KCl in a frequency from 0.1 to 10^5 Hz. Transmission electron microscopy (TEM) was measured by a Tecnai G20 transmission electron microscope (FEI Corporation, USA). Scanning electron microscopy (SEM) and energy-dispersive spectroscopy (EDS) were obtained with an S-4800 scanning electron microscope (Hitachi Instrument, Japan). Fourier transformed infrared (FT-IR) spectroscopy was obtained with a Spectrum One Fourier transformed infrared spectroscope (PerkinElmer, USA). X-ray diffraction (XRD) was recorded on a D8 Advance X-ray diffractometer (Bruker Corporation, Germany). Zeta potential was measured through Zetasizer Nano ZS90 (Malvern, Britain). X-ray photoelectron spectroscopy (XPS) was monitored on an Escalab 250Xi X-ray photoelectron spectroscope (Thermo Fisher Scientific, USA). An UV−vis spectroscope was obtained with a UV-3600 UV−vis spectrophotometer (Shimadzu, Japan). Nitrogen adsorption−desorption measurements was performed on a volumetric gas sorption instrument QDS-MP-30 (Quantachrome Instruments, USA).

Synthesis of PtPd NPs-GR. For the synthesis PtPd NPs-GR,[28] 100 μL of H_2PtCl_4 solution (50 mM) and 100 μL of K_2PdCl_4 solution (20 mM) were added to 1 mL of GR solution (0.17 mg/mL, pH 11). After being adsorbed for 24 h, 600 μL of freshly prepared $NaBH_4$ (50 mM) was slowly added to the solution with vigorous stirring for 1 h. The resulting products were centrifugated and washed with deionized water three times. The obtained PtPd NPs-GR was finally redispersed in 1 mL of CTAB (2 mM).

Preparation of MOFs (UiO-66-NH_2) and MB@DNA/MOFs. The MOFs were synthesized based on the previously reported method with minor modification.[29] In a typical synthesis, 40 mg of $ZrCl_4$ and 31 mg of NH_2-BDC were dissolved in 10 mL of DMF, and the mixture was ultrasonically treated for 5 min with the addition of 1 mL of acetic acid. After that, the solution was kept in a 50 mL Teflon liner and reacted at 120 °C for 24 h. After that, the resulting solution was treated with centrifugation at 9000 rpm, and the precipitates were washed with DMF and ethanol. Finally, the obtained MOFs were dried and stored for further use.

The as-synthesized MOFs were used to prepare MB@DNA/MOFs.[25] First, 10 μL of B-DNA1 (10 μM) and 100 μL of B-DNA2 (10 μM) were added to 500 μL of aqueous solution with 400 mM EDC and 100 mM NHS and then reacted for 1 h at room temperature. Afterward, 500 μL of MOFs (1 mg/mL) were mixed with the above solution and reacted for 3 h at room temperature. Then, the mixture was centrifugated at 10,000 rpm and rinsed with 10 mM PBS (pH 7.4) three times. Finally, the DNA-modified MOFs were redispersed and applied for the loading of signal molecules (MB). Fifty microliters of the MB solution (10 mM) was added to 1 mL of DNA-functionalized MOFs and kept stirred for 12 h, and then, 100 μL of L-DNA (10 μM) was introduced into the above solution and incubated at 37 °C for 1 h. Finally, the obtained DNA-gated MOFs were collected by centrifugation at 10,000 rpm and redispersed in PBS (10 mM, pH 7.4) for further use.

Fabrication of the Biosensor. The bare GCE was first burnished with γ-Al_2O_3 and ultrasonically treated with ethanol and deionized water three times. Then, 5 μL of PtPd NPs-GR was dropped onto the cleaned GCE and underwent natural drying. After that, the electrode was incubated with 1 μM CP for 12 h at room temperature and then incubated with 1 mM MCH to block the remaining sites. Subsequently, the modified electrode was incubated with MB@DNA/MOFs for 2 h at 37 °C. Meanwhile, 1 μM HP1 was incubated at a different concentration of CEA at 37 °C for 1 h. Then, the formed CEA/HP1 complex was incubated with 1 μM HP2 containing 5 U Nt.AlwI at 37 °C for 2 h to complete the nicking endonuclease cleavage process followed by a mixture that was heated at 80 °C for 10 min to inactivate Nt.AlwI. Thereafter, the MB@DNA/MOF-modified electrode was immersed into the mixture containing the cleavage product and 1 μM R-DNA for another 2 h at 37 °C to

DOI: 10.1021/acsami.9b18805
ACS Appl. Mater. Interfaces 2020, 12, 2087−2094

Scheme 1. Scheme Diagram of the DNA-Gated MOF-Based Electrochemical Biosensing Platform of CEA. (A) Assembly Procedure of MB@DNA/MOFs. (B) Target-Triggered Nicking Endonuclease Cleavage Process. (C) Signal Molecule Release from MB@DNA/MOFs on the Electrode

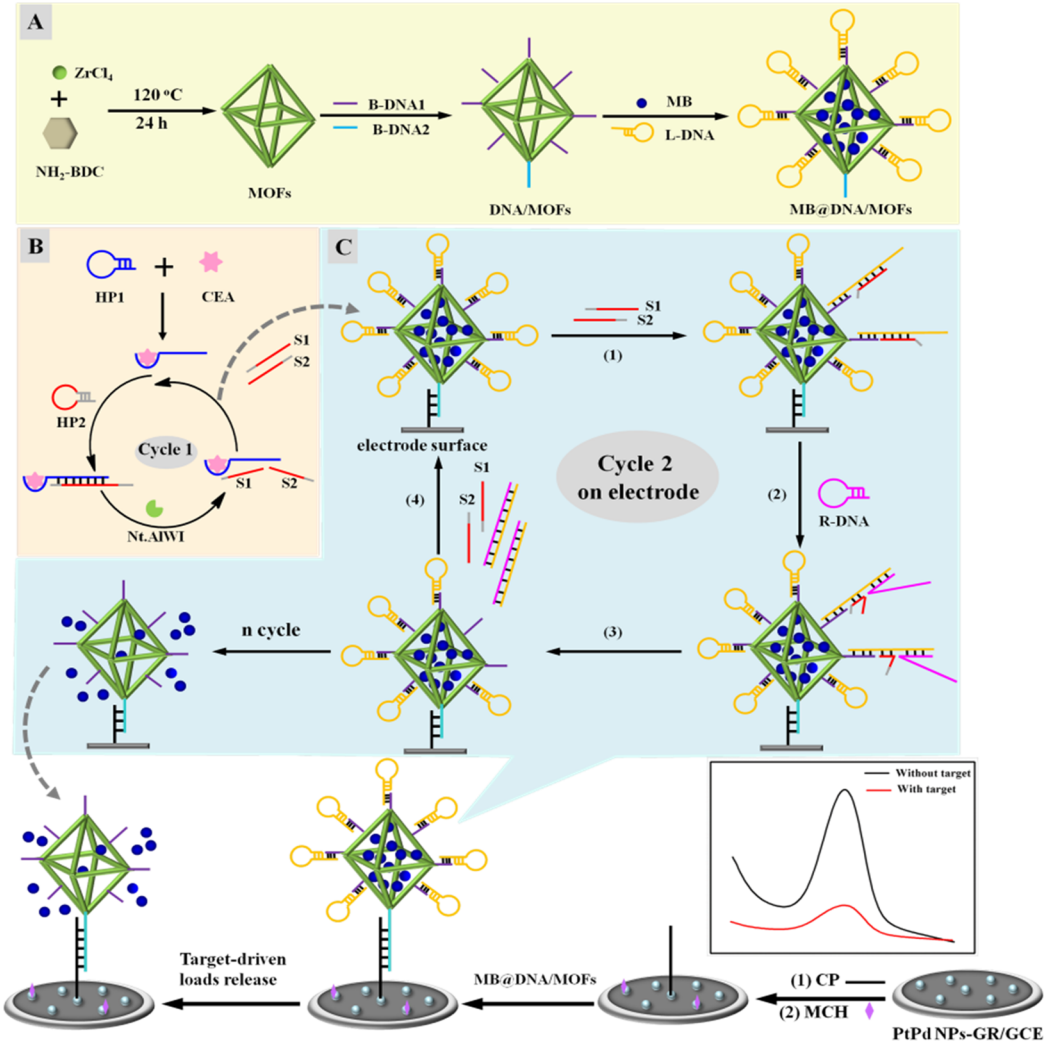

perform the SDR process. Ultimately, the electrode was used for electrochemical measurements in Tris−HCl (20 mM, pH 7.4).

RESULTS AND DISCUSSION

Principle of Stimuli-Responsive MOF-Based Electrochemical Biosensor. The ultrasensitive electrochemical biosensor for CEA detection was designed based on DNA-gated MOFs coupling with target-driven cascade amplification for load release (Scheme 1). The functionalized MOFs (MB@DNA/MOFs) were synthesized by the coordination of Zr^{4+} and NH_2-BDC, which were used as nanocarriers for electroactive MB encapsulation (Scheme 1A). First, the carboxylated B-DNA1 and B-DNA2 assembled on MOFs through the amidation reaction, which was followed by the load of MB into the pores of MOFs. Then, L-DNA assembled with B-DNA1 to act as the gatekeeper to form MB@DNA/MOFs, which modified on the electrode through the hybridization of B-DNA2 with CP on the electrode, which produced an arresting electrochemical signal due to the plentiful MB encapsulation. In the presence of CEA, HP1 recognized CEA to form an HP1-CEA complex, with an exposed segment to trigger the nicking endonucleases cleavage process (Scheme 1B), in which HP1-CEA hybridized with HP2 to form HP1-CEA-HP2 containing the nicking site of Nt.AlwI (5′-GGATCNNNN▼N-3′),[30] which specifically recognized the site and cleaved HP2 into two parts (S1 and S2) with the release of CEA-HP1 for recycling (cycle 1). With the completion of cycle 1, numerous S1 and S2 containing a length of the same sequence were generated to participate in the SDR process on MB@DNA/MOFs (Scheme 1C). In the SDR process, both S1 and S2 can hybridize with L-DNA, and the exposed segment acted as a toehold for R-DNA assembly. R-DNA was complementary with L-DNA to release S1 and S2 for recycling (cycle 2). With the cascade recycling proceeding, the capped L-DNA was dissociated from MB@DNA/MOFs, which induced the unlocking of the pore and the release of MB, resulting in the decrease of electrochemical signal. Consequently, the stimuli-responsive DNA-gated MOF-based electrochemical biosensor realized the detection of CEA.

Characterization of the Nanomaterials. Compared with bare GR (Figure 1A), the TEM image of PtPd NPs-GR (Figure 1B) also could be observed with the typical two-dimensional nanosheet structure of GR, and the well-dispersed PtPd NPs with a diameter of 5 nm was visible on the surface of GR. In addition, the XPS spectrum of PtPd NPs-GR is displayed in Figure S1, and the Pt 4f (73.5 eV) and Pd 3d

DOI: 10.1021/acsami.9b18805
ACS Appl. Mater. Interfaces 2020, 12, 2087−2094

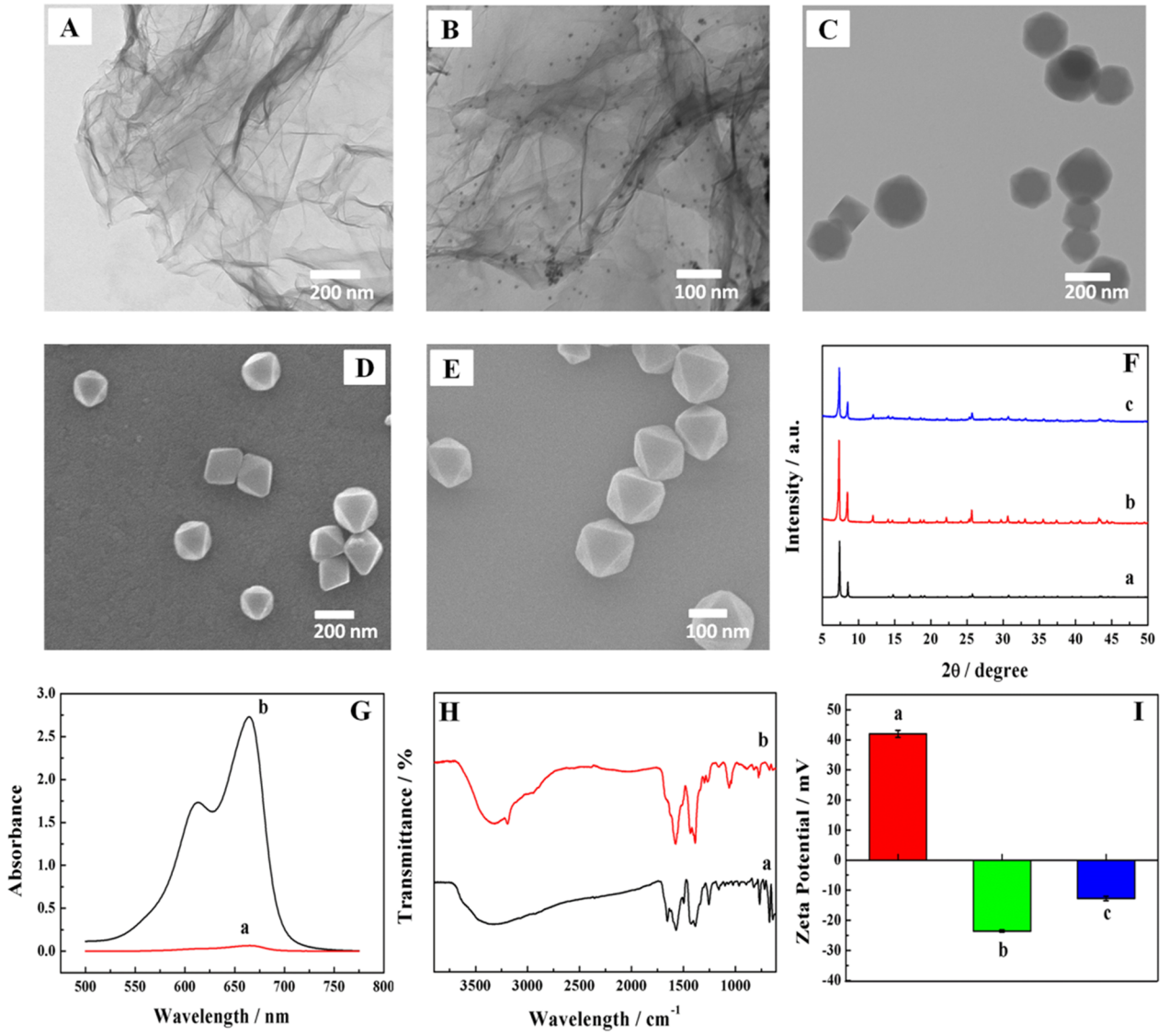

Figure 1. (A) TEM image of bare GR. (B) TEM image of PtPd NPs-GR. (C) TEM image of MOFs (UiO-66-NH_2). (D) SEM image of MOFs. (E) SEM image of MB@DNA/MOFs. (F) XRD patterns of (a) simulated MOFs, (b) the synthesized MOFs, and (c) MB@DNA/MOFs. (G) UV−vis spectrum of MB solution (curve a) and the supernatants of MB solutions after encapsulation by DNA/MOFs (curve b). (H) FT-IR spectrum of (a) MOFs and (b) MB@DNA/MOFs. (I) Zeta potential of (a) MOFs, (b) DNA/MOFs, and (c) MB@DNA/MOFs.

(332.3 eV) lines further proved the formation of PtPd NPs on GR.[31] The TEM image showed that the obtained MOFs were relatively uniform with a diameter of 170−200 nm (Figure 1C). In addition, the SEM image (Figure 1D) exhibited the characteristic octahedral structure of the synthesized MOFs.[32] The SEM image of MB@DNA/MOFs is shown in Figure 1E, which is similar with that of MOFs, proving that the morphology of MOFs had no obvious change with the loading of DNA and MB. Besides, XRD was applied to further confirm the synthesized MOFs and MB@DNA/MOFs. As shown in Figure 1F, compared with the simulated diffraction patterns of UiO-66-NH_2 (curve a), the synthesized MOFs (curve b) and MB@DNA/MOFs (curve c) presented similar patterns, which indicated that the structure of MOFs had no obvious change with the loading of DNA and MB.[33]

Furthermore, the UV−vis spectrum was conducted to check the successful loading of MB. As shown in Figure 1G, the absorption peaks of MB solution at 664 nm was significant (curve a), and the absorbance intensity of the supernatant obviously decreased after MB was incubated with DNA/MOFs (curve b), which proved the successful loading of MB into the MOFs. Besides, the UV−vis spectrum of MB@DNA/MOFs was also checked (Figure S2), which showed a similar absorption peak compared with that of MB. Moreover, the pore size of DNA/MOFs was investigated through a nitrogen adsorption−desorption experiment. As shown in Figure S3, the pore size distribution of DNA/MOFs presented a main peak at 1.6 nm. Furthermore, the molecule size of MB was 1.3−1.5 nm,[34] which was smaller than the pore size of DNA/MOFs. Therefore, MB can be loaded into the pores of DNA/MOFs to form MB@DNA/MOFs. In addition, the photo images of MB, MOFs, and MB@DNA/MOFs are presented in Figure S4; it could be seen that the MB@DNA/MOFs had the characteristic blue color of MB, which also proved the successful encapsulation of MB. Moreover, FT-IR was further used to validate the formation of MB@DNA/MOFs. As seen in Figure 1H, compared with the FT-IR spectrum of bare MOFs (curve a), the MB@DNA/MOFs (curve b) showed an imidyl bond

DOI: 10.1021/acsami.9b18805
ACS Appl. Mater. Interfaces 2020, 12, 2087−2094

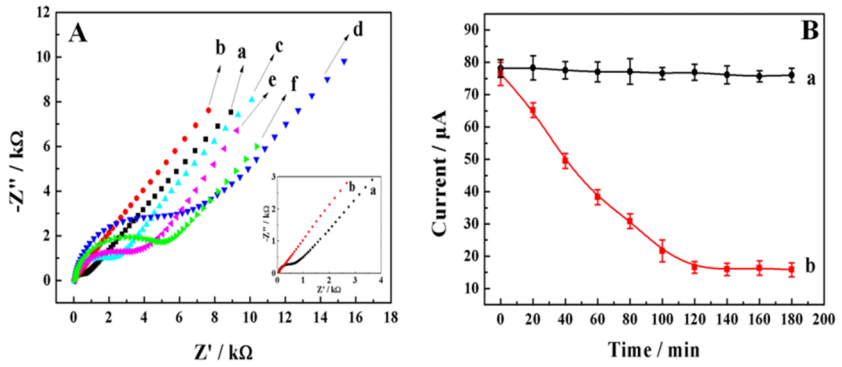

Figure 2. (A) EIS response of the modification steps of the biosensor: (a) bare GCE, (b) PtPd NPs-GR/GCE, (c) CP/PtPd NPs-GR/GCE, (d) MCH/CP/PtPd NPs-GR/GCE, (e) MB@DNA/MOFs modified from (d), and (f) (e) after the completion of nicking endonuclease cleavage and SDR process. (B) DPV response of the biosensor for the target-driven load release: (a) without the addition of CEA and (b) in the presence of 5 ng/mL CEA.

(1675 cm^{-1}) and a C−S bond (1050 cm^{-1}) due to the amidation reaction and the encapsulated MB, respectively. The assemble process of MB@DNA/MOFs was also verified by zeta potential. As shown in Figure 1I, the zeta potential of bare MOFs was +42 mV (column a), which decreased to −23.6 mV after the modification of B-DNA1 and B-DNA2 (column b), proving the successful assembly of DNA on MOFs. After the loading of MB into the pores of MOFs, the zeta potential was −13.8 mV (column c), which showed an increase due to the positive charge of MB.[35]

Characterization of the Biosensor. The modification steps of the biosensor were characterized by EIS, and the semicircle diameter of EIS was equal to electron transfer resistance (R_{et}). As seen in Figure 2A, compared with R_{et} (919.8 Ω) of bare GCE (curve a), the PtPd NPs-GR-modified electrode (curve b) showed a smaller R_{et} (60.22 Ω) due to the good conductivity of PtPd NPs-GR. An obvious increase of the R_{et} (3.123 kΩ) could be observed with the assembly of CP (curve c), which proved the successful assembly of CP. The R_{et} (5.704 kΩ) further increased after treated with MCH (curve d). With the modification of MB@DNA/MOFs, the R_{et} (3.755 kΩ) decreased (curve e), which was due to the presence of numerous electroactive MBs. After the electrode performed with the nicking endonuclease cleavage and SDR process, the R_{et} (4.612 kΩ) increased due to the effusion of MB (curve f). These EIS results confirmed the successful construction of the MOF-based biosensor.

Furthermore, the layered modification process of the electrode was proven by SEM. As shown in Figure S5A, the bare GCE presented a flat surface. With the modification of PtPd NPs-GR, characteristic morphology of GR and distributed PtPd NPs could be observed (Figure S5B). With the assembly of CP (Figure S5C), the CP-modified PtPd NPs-GR still kept the similar morphology, and the SEM-EDS mapping of CP-modified PtPd NPs-GR was further used to prove the CP assembly. As seen in Figure S6, the SEM-EDS mapping of elemental distributions presented the uniform distribution of P elements, which indicated the successful assembly of CP on the PtPd NPs-GR surface. With the addition of MCH, the morphology had no obvious change (Figure S5D). After the hybridization of MB@DNA/MOFs on the electrode, it could be observed with the presence of MB@DNA/MOFs on the surface of PtPd NPs-GR (Figure S5E). In addition, after the target-driven load process (Figure S5F), the similar morphology still could be observed compared with before the target-driven load release process.

In addition, the MB encapsulation effect and the target-driven load release of the biosensor were investigated. As shown in Figure 2B, the MB@DNA/MOF-modified electrode had a markedly electrochemical response without the addition of CEA, which was due to the numerous encapsulated MBs to produce an amplified signal (curve a). In addition, the DPV response had no obvious change with the extension of incubation time, which proved the good encapsulation effect of DNA-gated MOFs. With the presence of 5 ng/mL CEA, the electrochemical response gradually decreased with the increasing incubation time and it reached a plateau after 2 h (curve b). The signal decrease of the biosensor was attributed to the target-activated nicking endonuclease cleavage and SDR process, which caused the unlocking of the pore and the effusion of MB.

Optimization of Experimental Conditions. The assembled B-DNA1 and B-DNA2 on MOFs were important to the encapsulation effect of MB@DNA/MOFs; thus, the dosage ratio of B-DNA1 and B-DNA2 for MB@DNA/MOFs was optimized. As shown in Figure S7A, different volume ratios (2:1, 3:2, 1:10, and 1:5) of B-DNA1 (10 μM) and B-DNA2 (10 μM) were investigated, and the DPV response of the modified electrode had the most significant DPV response with a ratio of 1:10. Therefore, the optimal ratio of B-DNA1 and B-DNA2 was chosen to be 1:10. Besides, the dosage of MB was important for the signal output of the MB@DNA/MOF-modified electrode; thus, different dosages (10, 20, 40, 50, 60, and 80 μL) of 10 mM MB were investigated. As shown in Figure S7B, the DPV response of the biosenor increased with the increase of the MB dosage and kept stable with the addition of a 50 μL MB. Therefore, 50 μL was used as the optimal dosage of MB. In addition, the formation of the HP1-CEA complex could trigger the endonuclease cleavage process; hence, the effect of the recognition time between HP1 and CEA on the response of the biosensor was investigated. As shown in Figure S7C, the DPV current decreased gradually with the increase of incubation time and then became stable after 60 min. Hence, 60 min was selected as the optimal recognition time. Furthermore, the optimal incubation time for the nicking endonuclease cleavage process was also examined. As displayed in Figure S7D, the current response decreased with the increasing incubation time from 10 to 120 min and

DOI: 10.1021/acsami.9b18805
ACS Appl. Mater. Interfaces 2020, 12, 2087−2094

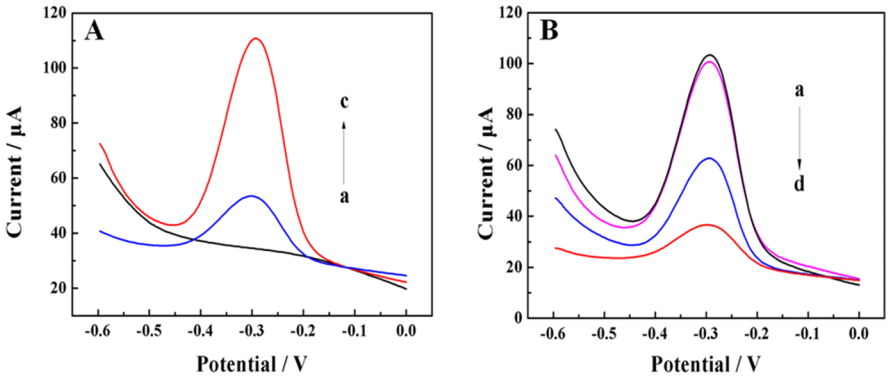

Figure 3. Amplification effect of the biosensor: (A) DPV response of the biosensor (a) with the modification of DNA/MOFs, (b) MB@DNA/MOFs without the presence of L-DNA, and (c) MB@DNA/MOFs with the presence of L-DNA. (B) DPV response of the biosensor of (a) MB@DNA/MOF-modified electrode, (b) without the presence of CEA, (c) with the addition of 5 ng/mL CEA and the SDR process, and (d) with the further introduction of 5 U Nt.AlwI.

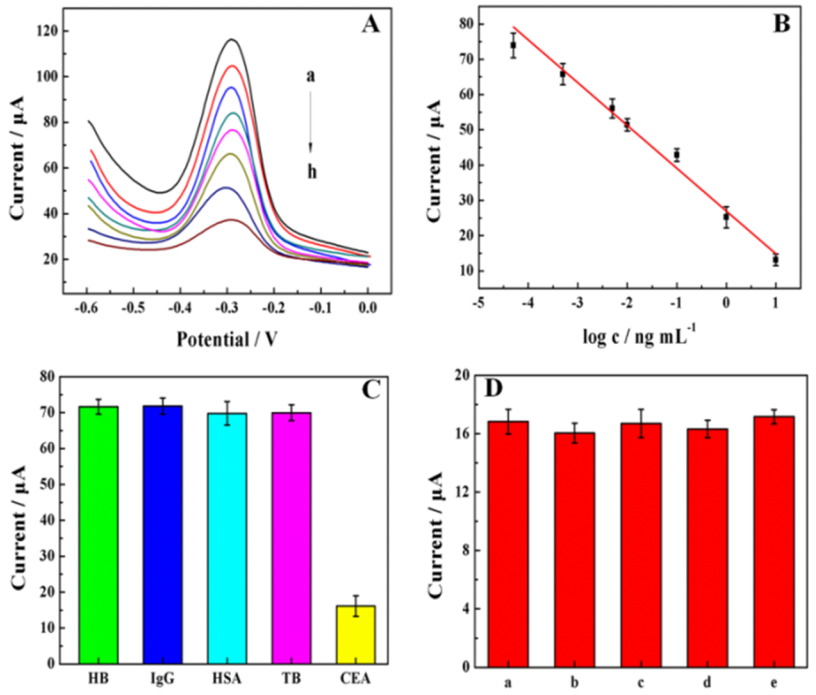

Figure 4. (A) DPV responses of the biosensor toward different CEA concentrations (from a to h: 0 fg/mL, 50 fg/mL, 500 fg/mL, 5 pg/mL, 10 pg/mL, 0.1 ng/mL, 1 ng/mL, and 10 ng/mL) (B) Linear relationship between the electrochemical signal and the logarithm concentration of CEA. (C) Selectivity of the biosensor toward CEA (5 ng/mL) and four interfering proteins (50 ng/mL), including HB, IgG, HSA, and TB. (D) DPV response of the five same-prepared biosensors for 5 ng/mL CEA detection.

reached a plateau after 120 min. Therefore, the optimal cleavage time was set to be 120 min.

Amplification Effect of the Biosensor. To prove the amplification performance of DNA-gated MOFs, different probes including DNA/MOFs, MB@DNA/MOFs with and without the presence of gated DNA were used for the modification of electrode separately, and the electrochemical signal was recorded. As shown in Figure 3A, the DPV response of the biosensor was negligible with the modification of DNA/MOFs (curve a). Without L-DNA, the MB@DNA/MOF-modified electrode still showed a small DPV response (curve b). However, there was a prominent electrochemical signal output for the MB@DNA/MOFs with the presence of L-DNA (curve c), which was due to the DNA/MOFs that provided abundant loading sites for electroactive MB.

In addition, the amplification effect of the cascade target recycling was investigated (Figure 3B). The MB@DNA/MOF-modified electrode had a significant electrochemical response (curve a), which was ascribed to the plentiful encapsulated MB that produced the amplified signal. Without the presence of CEA, the DPV response of the biosensor was still conspicuous (curve b), which was due to the locking state of the MB@DNA/MOFs. With the addition of 5 ng/mL CEA but without Nt.AlwI, the DPV signal decreased the formed HP1-CEA-HP2 that participated in the SDR process to cause the unlocking of the pore, and MB was released from MOFs to decrease the signal (curve c). With the further introduction of 5 U Nt.AlwI, the electrochemical response further decreased due to the nicking endonuclease cleavage process that generated abundant S1 and S2 to facilitate the SDR process, which resulted in the prominent decrease of the DPV signal (curve d). These

DOI: 10.1021/acsami.9b18805
ACS Appl. Mater. Interfaces 2020, 12, 2087−2094

experimental results proved the amplification effect of the cascade target recycling.

Analytical Performance of the Biosensor. Under optimal experimental conditions, the analytical performance of the biosensor for CEA detection was investigated (Figure 4). As shown in Figure 4A, compared with the blank sample (curve a), the DPV response of the biosensor decreased with extending concentration of CEA, ranging from 50 fg/mL to 10 ng/mL (curves b to h), which was due to the fact that more target caused more release of MB. Furthermore, the DPV current exhibited a good linear relationship toward the logarithm concentration of CEA (Figure 4B), and the linear equation was expressed as I (μA) = −12.13 lg c + 26.98 (ng/mL) (R = 0.9906), with a detection limit of 16 fg/mL (S/N = 3). Furthermore, the performance of the proposed biosensor toward CEA was compared with the reported methods (Table S2), which was more superior with a wider detection range and a lower detection limit, attributed to the DNA-gated MOFs with target-driven cascade amplification.

Selectivity, Reproducibility, and Stability of the Biosensor. The selectivity of the proposed biosensor was evaluated by recording the DPV response toward interfering proteins, including HB, IgG, HSA, and TB. As shown in Figure 4C, the electrochemical signal had no obvious change with the presence of four interfering proteins (50 ng/mL). However, the addition of CEA (5 ng/mL) caused an obvious decrease of the DPV response, indicating that the proposed biosensor had a good selectivity toward CEA. The good selectivity of the biosensor was ensured by the CEA aptamer sequence in HP1,[36] and the proposed strategy could be easily extend for the detection of different cancer biomarkers by changing the aptamer sequence. The reproducibility of the biosensor was checked by measuring the response toward 5 ng/mL CEA using five electrodes prepared under the same conditions. As shown in Figure 4D, five electrodes showed a similar DPV signal with a relative standard deviation (RSD) of 2.6%, demonstrating that the biosensor had acceptable reproducibility. In addition, the stability of the biosensor was investigated by storing the prepared biosensor at 4 °C for 2 weeks and recorded the electrochemical response. As shown in Figure S8, the DPV signal still remained at 91.6% after 2 weeks of storage, indicating that the proposed biosensor has good stability.

Practical Application of the Biosensor. To verify the practical application of the biosensor, different concentrations of CEA (0.5, 0.1, and 0.05 ng/mL) were added into the 10-folded diluted human serum and detected by the proposed biosensor. As shown in Table S3, the recoveries were ranging from 98.0 to 102.1% with the relative standard deviations (RSDs) from 1.2 to 3.7%, which revealed the potential application of the proposed biosensor toward CEA detection in real biological samples for early cancer diagnosis.

CONCLUSIONS

In conclusion, we have designed a label-free electrochemical biosensing platform based on DNA-gated MOFs integrated with target-driven cascade amplification for load release. By utilizing UiO-66-NH_2 as a nanocarrier and DNA as a gatekeeper, the prepared MB@DNA/MOFs not only were used as an amplified signal label but also acted as effective biosensing tracks. The presence of target initiated the cascade target recycling, which caused the unlocking of the pores, and the electroactive MB was released to decrease the signal. The proposed biosensor realized sensitive and selective detection of CEA in a linear range from 50 fg/mL to 10 ng/mL with a detection limit of 16 fg/mL. The DNA-gated MOF-based three-dimensional biosensing platform with rational utilization of the cascade amplification provided a new biosensing pattern, which opened an avenue for sensitive detection of different biomarkers in clinical diagnosis.

ASSOCIATED CONTENT

Supporting Information

The Supporting Information is available free of charge at https://pubs.acs.org/doi/10.1021/acsami.9b18805.

Sequences of the oligonucleotides, the XPS spectrum of PtPd NPs-GR, the UV−vis spectrum of MB@DNA/MOFs, nitrogen adsorption−desorption measurements and pore size distribution of DNA/MOFs, the photo image of MB@DNA/MOFs, the SEM image of layered modification process of the biosensor; SEM-EDS mapping images of CP-modified PtPd NPs-GR, optimization of experimental conditions, stability of the biosensor, comparison of this strategy with other methods, and practical application of the proposed biosensor (PDF)

AUTHOR INFORMATION

Corresponding Author

*E-mail: wangsf@hubu.edu.cn. Tel: +86-27-50865309. Fax: +86-27-88663043.

ORCID

Wei Wen: 0000-0001-6138-7470

Xiuhua Zhang: 0000-0003-3586-9921

Shengfu Wang: 0000-0001-7175-4908

Notes

The authors declare no competing financial interest.

ACKNOWLEDGMENTS

This work was funded by the National Natural Science Foundation of China (grant no. 21775033).

REFERENCES

(1) Bray, F.; Ferlay, J.; Soerjomataram, I.; Siegel, R. L.; Torre, L. A.; Jemal, A. Global Cancer Statistics 2018: GLOBOCAN Estimates of Incidence and Mortality Worldwide for 36 Cancers in 185 Countries. *CA-Cancer J. Clin.* **2018**, *68*, 394−424.

(2) Henry, N. L.; Hayes, D. F. Cancer Biomarkers. *Mol. Oncol.* **2012**, *6*, 140−146.

(3) Guo, J.; Wang, J.; Zhao, J.; Guo, Z.; Zhang, Y. Ultrasensitive Multiplexed Immunoassay for Tumor Biomarkers Based on DNA Hybridization Chain Reaction Amplifying Signal. *ACS Appl. Mater. Interfaces* **2016**, *8*, 6898−6904.

(4) Chu, Y.; Deng, A. P.; Wang, W.; Zhu, J. J. Concatenated Catalytic Hairpin Assembly/Hyperbranched Hybridization Chain Reaction Based Enzyme-Free Signal Amplification for the Sensitive Photoelectrochemical Detection of Human Telomerase RNA. *Anal. Chem.* **2019**, *91*, 3619−3627.

(5) Xiao, M.; Man, T.; Zhu, C.; Pei, H.; Shi, J.; Li, L.; Qu, X.; Shen, X.; Li, J. MoS_2 Nanoprobe for MicroRNA Quantification Based on Duplex-Specific Nuclease Signal Amplification. *ACS Appl. Mater. Interfaces* **2018**, *10*, 7852−7858.

(6) Liu, J.; Cui, M.; Zhou, H.; Yang, W. DNAzyme Based Nanomachine for in Situ Detection of MicroRNA in Living Cells. *ACS Sens.* **2017**, *2*, 1847−1853.

DOI: 10.1021/acsami.9b18805
ACS Appl. Mater. Interfaces 2020, 12, 2087−2094

(7) Qiu, Z.; Shu, J.; Tang, D. Near-Infrared-to-Ultraviolet Light-Mediated Photoelectrochemical Aptasensing Platform for Cancer Biomarker Based on Core-Shell $NaYF_4$:Yb,Tm@TiO_2 Upconversion Microrods. *Anal. Chem.* **2018**, *90*, 1021−1028.
(8) Yang, S.-S.; Jiang, M.-H.; Chai, Y.-Q.; Yuan, R.; Zhuo, Y. Application of Antibody-Powered Triplex-DNA Nanomachine to Electrochemiluminescence Biosensor for the Detection of Anti-Digoxigenin with Improved Sensitivity Versus Cycling Strand Displacement Reaction. *ACS Appl. Mater. Interfaces* **2018**, *10*, 38648−38655.
(9) Zhang, X.; Yang, Z.; Chang, Y.; Qing, M.; Yuan, R.; Chai, Y. Novel 2D-DNA-Nanoprobe-Mediated Enzyme-Free-Target-Recycling Amplification for the Ultrasensitive Electrochemical Detection of MicroRNA. *Anal. Chem.* **2018**, *90*, 9538−9544.
(10) Furukawa, H.; Cordova, K. E.; O'Keeffe, M.; Yaghi, O. M. The Chemistry and Applications of Metal-Organic Frameworks. *Science* **2013**, *341*, 1230444−1230444.
(11) Li, B.; Wen, H.-M.; Cui, Y.; Zhou, W.; Qian, G.; Chen, B. Emerging Multifunctional Metal-Organic Framework Materials. *Adv. Mater.* **2016**, *28*, 8819−8860.
(12) Nandasiri, M. I.; Jambovane, S. R.; McGrail, B. P.; Schaef, H. T.; Nune, S. K. Adsorption, Separation, and Catalytic Properties of Densified Metal-Organic Frameworks. *Coord. Chem. Rev.* **2016**, *311*, 38−52.
(13) Zhu, L.; Liu, X.-Q.; Jiang, H.-L.; Sun, L. B. Metal-Organic Frameworks for Heterogeneous Basic Catalysis. *Chem. Rev.* **2017**, *117*, 8129−8176.
(14) Wu, M.-X.; Yang, Y.-W. Metal-Organic Framework (MOF)-Based Drug/Cargo Delivery and Cancer Therapy. *Adv. Mater.* **2017**, *29*, 1606134.
(15) Kumar, P.; Deep, A.; Kim, K.-H. Metal Organic Frameworks for Sensing Applications. *TrAC, Trends Anal. Chem.* **2015**, *73*, 39−53.
(16) Wu, S.; Li, C.; Shi, H.; Huang, Y.; Li, G. Design of Metal-Organic Framework-Based Nanoprobes for Multicolor Detection of DNA Targets with Improved Sensitivity. *Anal. Chem.* **2018**, *90*, 9929−9935.
(17) Liu, T.-Z.; Hu, R.; Zhang, X.; Zhang, K.-L.; Liu, Y.; Zhang, X.-B.; Bai, R.-Y.; Li, D.; Yang, Y.-H. Metal-Organic Framework Nanomaterials as Novel Signal Probes for Electron Transfer Mediated Ultrasensitive Electrochemical Immunoassay. *Anal. Chem.* **2016**, *88*, 12516−12523.
(18) Shen, H.; Liu, J.; Lei, J.; Ju, H. A Core-Shell Nanoparticle-Peptide@Metal-Organic Framework as pH and Enzyme Dual-Recognition Switch for Stepwise-Responsive Imaging in Living Cells. *Chem. Commun.* **2018**, *54*, 9155−9158.
(19) Liu, X.; Qi, W.; Wang, Y.; Su, R.; He, Z. A Facile Strategy for Enzyme Immobilization with Highly Stable Hierarchically Porous Metal-Organic Frameworks. *Nanoscale* **2017**, *9*, 17561−17570.
(20) Chen, D.-M.; Zhang, N.-N.; Liu, C.-S.; Du, M. Dual-Emitting Dye@MOF Composite as a Self-Calibrating Sensor for 2,4,6-Trinitrophenol. *ACS Appl. Mater. Interfaces* **2017**, *9*, 24671−24677.
(21) Yu, H.; Zhang, W.; Lv, S.; Han, J.; Xie, G.; Chen, S. A One-Step Structure-Switching Electrochemical Sensor for Transcription Factor Detection Enhanced with Synergistic Catalysis of PtNi@MIL-101 and Exo III-Assisted Cycling Amplification. *Chem. Commun* **2018**, *54*, 11901−11904.
(22) Ge, Z.; Gu, H.; Li, Q.; Fan, C. Concept and Development of Framework Nucleic Acids. *J. Am. Chem. Soc.* **2018**, *140*, 17808−17819.
(23) Feng, L.; Liu, M.; Liu, H.; Fan, C.; Cai, Y.; Chen, L.; Zhao, M.; Chu, S.; Wang, H. High-Throughput and Sensitive Fluorimetric Strategy for MicroRNAs in Blood Using Wettable Microwells Array and Silver Nanoclusters with Red Fluorescence Enhanced by Metal Organic Frameworks. *ACS Appl. Mater. Interfaces* **2018**, *10*, 23647−23656.
(24) Meng, H.-M.; Liu, H.; Kuai, H.; Peng, R.; Mo, L.; Zhang, X.-B. Aptamer-Integrated DNA Nanostructures for Biosensing, Bioimaging and Cancer Therapy. *Chem. Soc. Rev.* **2016**, *45*, 2583−2602.
(25) Kahn, J. S.; Freage, L.; Enkin, N.; Garcia, M. A. A.; Willner, I. Stimuli-Responsive DNA-Functionalized Metal-Organic Frameworks (MOFs). *Adv. Mater.* **2017**, *29*, 1602782−1602782.
(26) Cao, X.; Xia, J.; Meng, X.; Xu, J.; Liu, Q.; Wang, Z. Stimuli-Responsive DNA-Gated Nanoscale Porous Carbon Derived from ZIF-8. *Adv. Funct. Mater.* **2019**, *29*, 1902237−1902237.
(27) Chen, W.-H.; Yu, X.; Liao, W.-C.; Sohn, Y. S.; Cecconello, A.; Kozell, A.; Nechushtai, R.; Willner, I. ATP-Responsive Aptamer-Based Metal-Organic Framework Nanoparticles (NMOFs) for the Controlled Release of Loads and Drugs. *Adv. Funct. Mater.* **2017**, *27*, 1702102−1702102.
(28) Wang, W.; Bao, T.; Zeng, X.; Xiong, H.; Wen, W.; Zhang, X.; Wang, S. Ultrasensitive Electrochemical DNA Biosensor Based on Functionalized Gold Clusters/Graphene Nanohybrids Coupling with Exonuclease III-Aided Cascade Target Recycling. *Biosens. Bioelectron.* **2017**, *91*, 183−189.
(29) Ling, P.; Lei, J.; Jia, L.; Ju, H. Platinum Nanoparticles Encapsulated Metal-Organic Frameworks for the Electrochemical Detection of Telomerase Activity. *Chem. Commun.* **2016**, *52*, 1226−1229.
(30) Rauf, S.; Zhang, L.; Ali, A.; Ahmad, J.; Liu, Y.; Li, J. Nanopore-Based, Label-Free, and Real-Time Monitoring Assay for DNA Methyltransferase Activity and Inhibition. *Anal. Chem.* **2017**, *89*, 13252−13260.
(31) Shi, Y.-C.; Feng, J.-J.; Lin, X.-X.; Zhang, L.; Yuan, J.; Zhang, Q.-L.; Wang, A.-J. One-Step Hydrothermal Synthesis of Three-Dimensional Nitrogen-Doped Reduced Graphene Oxide Hydrogels Anchored PtPd Alloyed Nanoparticles for Ethylene Glycol Oxidation and Hydrogen Evolution Reactions. *Electrochim. Acta* **2019**, *293*, 504−513.
(32) Zhang, G.; Dong, H.; Zhang, X. Fluorescence Proximity Assay Based on a Metal-Organic Framework Platform. *Chem. Commun.* **2019**, *55*, 8158−8161.
(33) Chang, J.; Wang, X.; Wang, J.; Li, H.; Li, F. Nucleic Acid-Functionalized Metal-Organic Framework-Based Homogeneous Electrochemical Biosensor for Simultaneous Detection of Multiple Tumor Biomarkers. *Anal. Chem.* **2019**, *91*, 3604−3610.
(34) Attia, A. A.; Girgis, B. S.; Fathy, N. A. Removal of Methylene Blue by Carbons Derived from Peach Stones by H_3PO_4 Activation: Batch and Column Studies. *Dyes Pigm.* **2008**, *76*, 282−289.
(35) Yang, S.-T.; Chen, S.; Chang, Y.; Cao, A.; Liu, Y.; Wang, H. Removal of Methylene Blue from Aqueous Solution by Graphene Oxide. *J. Colloid Interface Sci.* **2011**, *359*, 24−29.
(36) Guo, C.; Su, F.; Song, Y.; Hu, B.; Wang, M.; He, L.; Peng, D.; Zhang, Z. Aptamer-Templated Silver Nanoclusters Embedded in Zirconium Metal-Organic Framework for Bifunctional Electrochemical and SPR Aptasensors toward Carcinoembryonic Antigen. *ACS Appl. Mater. Interfaces* **2017**, *9*, 41188−41199.

DOI: 10.1021/acsami.9b18805
ACS Appl. Mater. Interfaces 2020, 12, 2087−2094